Modelling of hot air chamber designs of a continuous flow grain dryer

Kjær, Lotte Strange; Poulsen, Mathias; Sørensen, Kim; Condra, Thomas Joseph

Published in:
Engineering Science and Technology, an International Journal

DOI (link to publication from Publisher):
10.1016/j.jestch.2018.02.002

Publication date:
2018

Document Version
Publisher's PDF, also known as Version of record

Engineering Science and Technology, an International Journal 21 (2018) 1047–1055

HOSTED BY

ELSEVIER

Contents lists available at ScienceDirect

Engineering Science and Technology, an International Journal

journal homepage: www.elsevier.com/locate/jestch

Full Length Article

Modelling of hot air chamber designs of a continuous flow grain dryer

Lotte Strange Kjær, Mathias Poulsen *, Kim Sørensen, Thomas Condra

Institute of Energy Technology, Aalborg University, Pontoppidanstræde 101, DK-9220 Aalborg, Denmark

ARTICLE INFO

Article history:
Received 9 June 2017
Revised 6 December 2017
Accepted 4 February 2018
Available online 25 July 2018

Keywords:
CFD
Fluid flow
Temperature distribution
Uniformity index
Continuous flow dryer
Grid convergence index

ABSTRACT

The pressure loss, flow distribution and temperature distribution of a number of designs of the hot air chamber in a continuous flow grain dryer, were investigated using CFD. The flow in the dryer was considered as steady state, compressible and turbulent. It is essential that the grain is uniformly dried as uneven drying can result in damage to the end-product during storage. The original commercial design was modified with new guide vanes at the inlets to reduce the pressure loss and to ensure a uniform flow to the line burner in the hot air chamber. The new guide vane design resulted in a 10% reduction in pressure loss and a γ-value of 0.804. Various design changes of the hot air chamber were analysed in terms of pressure loss and temperature distribution with the aim of a temperature variation of ±5 K at the outlet ducts. An obstruction design was analysed, which improved mixing and gave a temperature distribution within the limits. However, the pressure loss was six times larger than the original design with new guide vanes. Finally, The static mixer design resulted in a 23% reduction in the pressure loss, but had a mean absolute deviation of 22.9 K.

1. Introduction

Normally grain is harvested with a moisture content of 18–25% [1]. Therefore, post harvest treatment, in the form of drying, is needed in order to reduce the moisture content to 14% as this ensures safe storage of the grain. Typically the amount of energy used to remove water by evaporation from grain during drying is in excess 4.5 MJ/kg, whereas the amount of energy required to evaporate free water is only 2.3 MJ/kg and this makes the process of drying grain an energy intensive process [2]. Therefore, it is important to ensure that the drying process is as efficient as possible, while grain damage from drying is minimised.

In the current generation of continuous flow dryers, it has been observed that improper mixing of the air flows in the hot air chamber occurs. This causes significant variations in the temperature and flow distributions when the air enters the grain drying column. In Giner et.al. [3] a complex model of mixed-flow grain drying was developed where the two-dimensional flow patterns of the air and grain around the inlet and outlet air ducts in the drying column have been taken into account. As a result, it was found that heating and drying of the grain were more intense in the close proximity of the air ducts leading into the grain column. Thus, it is important to obtain a uniform temperature distribution to avoid over-drying of the grain near the air ducts. A design of the hot air chamber which can ensure a uniform temperature distribution into the grain column is therefore desirable.

There have been several studies on the air flow and temperature distribution in smaller dryer systems such as batch and cabinet dryers [4,5]. However, the studies are either performed on small or on laboratory scale dryers and in the literature the hot air chamber in a full scale continuous grain dryer is seldom investigated.

The purpose of this study is to identify a conceptual design that can be the basis for of further design improvements. These should reduce the variation in the drying air temperature at the outlet ducts. However, it is not desirable to increase the operation cost and so the pressure loss in the new design must be kept as low as possible.

2. Initial dryer design

A new conceptual design for a continuous flow grain dryer has been developed, and the hot air chamber will be the starting point for this study. The geometry of the hot air chamber, in the new design, is shown in Fig. 1.

The hot air chamber, seen in Fig. 1, consists of two ambient air inlets, where the ambient air is led into the hot air chamber by two axial fans. Correspondingly, air that has been used to cool the grain is recirculated into the hot air chamber through a sub-chamber. The recirculated air is then mixed with ambient air, that has been

* Corresponding author.
E-mail addresses: lottestrangekjaer@gmail.dk (L.S. Kjær), mps@et.aau.dk (M. Poulsen), kso@et.aau.dk (K. Sørensen), tc@et.aau.dk (T. Condra).

Peer review under responsibility of Karabuk University.

https://doi.org/10.1016/j.jestch.2018.02.002
2215-0986/

Nomenclature

Symbol	Description/Unit
A	Area [m^2]
e	Error [–]
GCI	Grid Convergence Index [–]
g	Grid size [m]
h	Enthalpy [J/kg]
k	Turbulent Kinetic Energy [m^2/s^2]
$\dot{m}$	Mass Flow [kg/s]
N	Number of cells [–]
r	Refinement Ratio [–]
p	Pressure [Pa]
P	Global Order of Accuracy [–]
s	Sign Factor [–]
T	Temperature [K]
U	Velocity [m/s]
v	Velocity Magnitude [m/s]
V	Volume [m^3]
x	Length [m]
γ	Uniformity Index [–]
μ	Viscosity [Pa · s]
ρ	Density [kg/m^3]
σ	Prandtl Number [–]
ϕ	Test Parameter [–]
ω	Specific Turbulent Dissipation Rate [1/s]

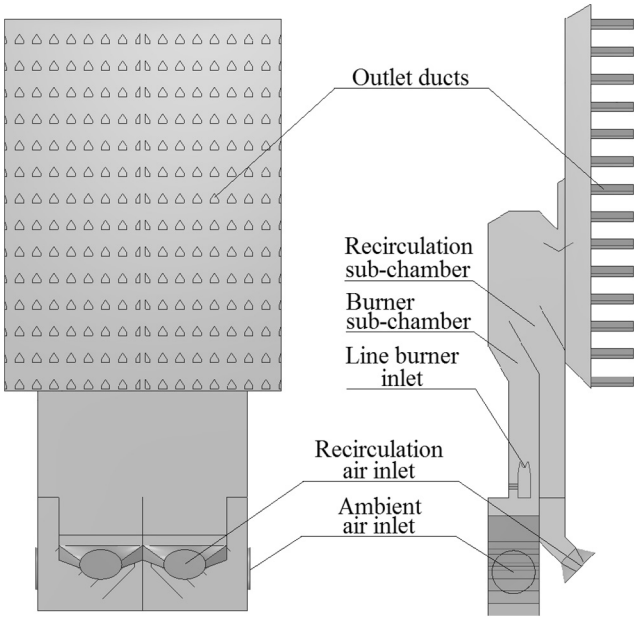

Fig. 1. Geometry of the hot air chamber.

heated by a line burner, at the end of the sub-chamber. The mixing is not carried out upstream of the burner, due to the presence of dust in the recirculation air, which, if passed through the burner, could result in a fire, or a dust explosion. After the two air streams have mixed, the air is led through a manifold, where it is distributed into the outlet air ducts. In the outlet air ducts the air is forced through the grain in the drying column.

3. Computational methodology

3.1. Solution domain

The solution domain has been simplified in order to reduce the number of cells needed to generate a proper mesh. Initially the interior baffles and guide vanes in the geometry were set as plates with a thickness of 2 mm, as this is the material thickness that will be used in the physical construction. However, when generating a mesh on the geometry some low quality elements were formed on the edges of all the baffles and guide vanes. Therefore, it was decided that all of the baffles and guide vanes should be modelled as thin surfaces instead, thereby eliminating poor quality elements. Furthermore, the sub-chamber to the right of the line burner was removed in the model, as no flow is present in the sub-chamber. The last simplification made to the solution domain was the removal of the area above the top baffle, as the flow in this area is not of interest.

3.2. Governing equations

The fluid flow in this study was assumed to be air in steady-state, compressible, and three-dimensional turbulent flow. The numerical calculation of the flow can be considered as mathematical formulations of the conservation laws of fluid mechanics. By applying the mass, momentum, and energy conservation, the fundamental governing equations of fluid dynamics; the mass (1) and momentum (Navier Stokes) (2), (3) equation can be written as follows [6]:

$$\frac{\partial(\rho U_i)}{\partial x_i} = 0 \tag{1}$$

where ρ is the density of the fluid, U_i are the Cartesian velocity component (i = 1, 2 and 3), x_i are the coordinate axes, and the repeated indices imply summation over 1–3.

$$U_j \frac{\partial(\rho U_i)}{\partial x_j} = -\frac{\partial p}{\partial x_i} + \frac{\partial}{\partial x_j}\left(\mu \frac{\partial U_i}{\partial x_j}\right) + \frac{\partial R_{ij}}{\partial x_j} \tag{2}$$

where p is the pressure, μ is the dynamic viscosity. The Reynolds stresses can be written as:

$$R_{ij} = \mu_t\left(U_j \frac{\partial(\rho U_i)}{\partial x_j}\right) - \frac{2}{3}\rho k \delta_{ij} \tag{3}$$

where μ_t is the eddy viscosity, k is the turbulent kinetic energy and δ_{ij} is the Kronecker symbol.

3.3. Turbulence modelling

The above equations are supplemented by a turbulence model to account for the turbulence in the flow. In the present case, the Shear Stress Transport (SST) k-ω model has been used, as it combines the advantages of the k-ε model in the far-field region and the k-ω model in the near-wall region [7]. The turbulent flow is computed in terms of two additional parameters, i.e. the turbulent kinetic energy, k, and the specific turbulent dissipation rate, ω. The turbulent kinetic energy and the specific dissipation rate are computed using Eqs. (4) and (5), respectively [6,8]:

$$\frac{\partial(\rho k u_i)}{\partial x_i} = \frac{\partial}{\partial x_j}\left(\Gamma_k \frac{\partial k}{\partial x_j}\right) + \widetilde{G}_k - Y_k + S_k \tag{4}$$

$$\frac{\partial(\rho \omega u_i)}{\partial x_i} = \frac{\partial}{\partial x_j}\left(\Gamma_\omega \frac{\partial \omega}{\partial x_j}\right) + G_\omega - Y_\omega + D_\omega + S_\omega \tag{5}$$

where Γ_k and Γ_ω are the effective diffusivity of k and ω, $\widetilde{G}_k$ is the generation of turbulent kinetic energy caused by mean velocity gradients, G_ω is the generation of ω, Y_k and Y_ω are the dissipations of k and ω due to turbulence, D_ω is the cross-diffusion term and S_k and S_ω are the user-defined source terms.

The effective diffusivities for the SST k-ω model are determined using the following expressions [7,6]:

$$\Gamma_k = \mu + \frac{\mu_t}{\sigma_k} \tag{6}$$

$$\Gamma_\omega = \mu + \frac{\mu_t}{\sigma_\omega} \tag{7}$$

where σ_k and σ_ω are the turbulent Prandtl numbers for k and ω, respectively. They are determined using the following equations [7,6]:

$$\sigma_k = \frac{1}{\frac{F_1}{\sigma_{k,1}} + \frac{(1-F_1)}{\sigma_{k,2}}} \tag{8}$$

$$\sigma_\omega = \frac{1}{\frac{F_1}{\sigma_{\omega,1}} + \frac{(1-F_1)}{\sigma_{\omega,2}}} \tag{9}$$

where F_1 is a blending function.

The turbulent viscosity μ_t is computed using the following expression:

$$\mu_t = \frac{\rho k}{\omega} \frac{1}{\max\left[\frac{1}{\alpha^*}, \frac{S \cdot F_2}{a_1 \cdot \omega}\right]} \tag{10}$$

where α^* is a damping coefficient for turbulent viscosity, $S = \sqrt{2 S_{ij} S_{ij}}$ is an invariant measure of the strain rate with S_{ij} being the mean strain rate tensor, a_1 is a constant and F_2 is a blending function.

3.4. Temperature

To have a temperature reference in the air duct outlets, it has been assumed that complete mixing of the different air streams occurs. This allows the temperature of the mixed air streams to be given as:

$$\begin{aligned} h_{i,n} &= \frac{\sum_{i=1}^{n} h_i \cdot \dot{m}_i}{\sum_{i=1}^{n} \dot{m}_i} \\ T_{i,n} &= f\left(h_{i,n}\right) \end{aligned} \tag{11}$$

where $h_{i,n}$ is the enthalpy of combined air stream, h_i is the enthalpy of individual air stream, and $\dot{m}_i$ is the mass flow of individual air stream.

The expressions described in Sections 3.2 and 3.3 are nonlinear partial differential equations and these expressions are solved numerically using the computer code ANSYS Fluent, ver. 17.2. The accuracy of the numerical solution is contingent on how well the discretised equations depict the original partial differential equations. ANSYS Fluent applies the finite volume method to discretise the partial differential equations and uses a non-staggered grid approach, where the values of the variables are computed at the centre of the cells [8]. The governing equations are discretised using the second-order Upwind scheme. The COUPLED algorithm is utilised to link the velocity and pressure, where the pressure term is discretised using the second-order scheme.

3.5. Mesh generation

All meshing performed in this study was accomplished using CutCell assembly meshing from ANSYS Meshing ver. 17.2 [8]. The major advantages of the CutCell method is that it reduces the time needed to mesh complex geometries and usually results in high quality hexahedral mesh elements, which commonly leads to a faster solution convergence. It was not possible to generate a global boundary layer using the Cutcell method. The cell size, on the internal surfaces of the solution domain, was instead significantly reduced in an effort to represent the presence of a boundary layer. The mesh generated at the guide vanes in the bottom of the hot air chamber is shown in Fig. 2.

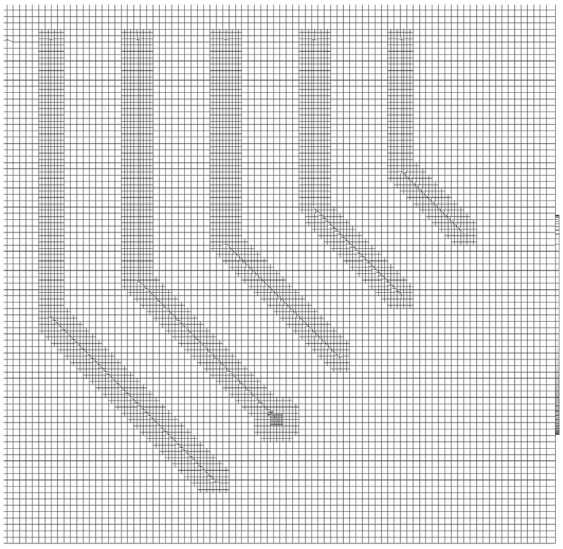

Fig. 2. Generated mesh at the guide vanes.

3.6. Boundary conditions and assumptions

The line burner has a high air excess ratio, and is essentially a row of gas jets on a pipe with the combustion air flowing around the pipe. To simplify the computation and to limit cell usage at the line burner, the combustion process at the line burner is neglected. The combustion process is instead approximated by air at 1500 °C, which correspond to the temperature of the combustion products. Furthermore, the walls are assumed to be adiabatic, meaning that there is no heat transfer between the hot air, inside the air chamber, and the ambient air. Under real operating condition the axial fans installed at both the ambient air inlet and the recirculation air inlet, might result in an uneven and swirling velocity profile at the inlets. As the velocity profiles of the axial fans are not known, it would require a secondary study to acquire the profiles. Therefore, it is assumed that the velocity profile at the inlet resembles a plug flow. The inlet conditions have been provided by a commercial source. The values presented in Table 1 are for a half hot air chamber.

3.6.1. Symmetry

It is seen in Fig. 1 that the solution domain has a symmetry plane between the two recirculation air inlets. It has been investigated, whether it was reasonable to model half the hot air chamber with a symmetry plane instead of the full-sized chamber, in further simulations of the hot air chamber. This was done by examining the temperature and mass flow in the outlet air ducts on each half of the symmetry plane. This was also done for different plane cuts taken in the solution domain. It was found that there was good agreement between the temperature and mass flows in the two symmetry halves, except for five of the outlet air ducts, where the temperature difference ranged between 38 and 20 K. However,

Table 1
Boundary conditions for the hot air chamber.

Boundary	Mass flow [kg/s]	Temperature [°C]
Ambient air inlet	16.8	15
Recirculation air inlet	21	40
Line burner inlet	1.5	1500

the benefits of improved mesh quality, cell count and computational time when using the symmetry model outweighed the differences present, when modelling the full-sized hot air chamber.

4. Verification

4.1. Grid convergence test

A grid convergence test on the solution domain has been conducted. As it is important to keep the pressure loss in the new design at a minimum, and because the pressure loss is global for the domain, it has been chosen as the test parameter when testing for grid convergence. The pressure loss is determined as the difference in the area weighted average of the total-pressure in the ambient air inlets and the outlets. Three progressively finer unstructured grids of the solution domain have been created for the test. The number of cells in the grids and the pressure loss for each, can be seen in Table 2.

The test has been performed with the Grid Convergence Index (GCI) [9,10]. This method is widely utilised across different areas in the CFD community [11], as it provides a uniform way of reporting the accuracy of the grid independence test. The GCI method utilises Richardson's extrapolation to estimate the value of the test parameter (ϕ) when the grid spacing approaches zero, and provides a 2σ error band, for the approximated value. The procedure for estimating the GCI for the different meshes can be summarised as follows:

1. Define the refinement ratio between the grids. To define the refinement ratio, a measure of the cell size must be determined:

$$g_i = \left[\frac{1}{N}\sum_{j=1}^{N}\Delta V\right]^{\frac{1}{3}} \tag{12}$$

where g is the grid size, N is the number of cells in the domain and ΔV is the volume of the individual cell. The refinement ratio can then be defined as:

$$r_{ij} = \frac{g_i}{g_j} \tag{13}$$

2. Calculate the apparent global order of accuracy.
The apparent global order of accuracy is solved in an iterative process, as the refinement ratio between the first and second grid, is not the same as the second and third grid. The apparent global order of accuracy can be given as:

$$P = \frac{1}{\ln(r_{21})}\left|\ln\left(\left|\frac{\epsilon_{32}}{\epsilon_{21}}\right|\right) + q(P)\right| \tag{14}$$

where P is the apparent global order of accuracy and $\epsilon_{ij} = \phi_i - \phi_j$.

Table 2
Number of cells and pressure loss in grids for solution domain.

Grid	Number of cells	Pressure loss [Pa]
1	$4.568 \cdot 10^6$	700
2	$3.039 \cdot 10^6$	692
3	$2.484 \cdot 10^6$	671

Table 3
Results from the GCI test.

Variable	Value	Variable	Value
r_{21}	1.14	e_a^{21}	1.1%
r_{32}	1.07	e_{ext}^{21}	3.7%
P	1.88	GCI_{fine}^{21}	4.7%
Δp_{ext}^{21}	727 [Pa]		

$$q(P) = \ln\left(\frac{r_{21}^P - s}{r_{32}^P - s}\right) \tag{15}$$

$$s = 1 \cdot \mathrm{sign}\left(\frac{\epsilon_{32}}{\epsilon_{21}}\right) \tag{16}$$

3. Calculate the extrapolated value.

$$\phi_{ext}^{21} = \frac{r_{21}^P \phi_1 - \phi_2}{r_{21}^P - 1} \tag{17}$$

4. Calculate the estimation errors and GCI.

$$e_a^{21} = \left|\frac{\phi_1 - \phi_2}{\phi_1}\right| \tag{18}$$

where e_a^{21} is the approximate relative error.

$$e_{ext}^{21} = \left|\frac{\phi_{ext}^{21} - \phi_1}{\phi_{ext}^{21}}\right| \tag{19}$$

where e_{ext}^{21} is the extrapolated relative error.

$$\mathrm{GCI}_{fine}^{21} = \frac{1.25 e_a^{21}}{r_{21}^P - 1} \tag{20}$$

where GCI_{fine}^{21} is the fine grid convergence index.

The results of the GCI test is shown in Table 3.

It is recommended that r_{ij} is greater than 1.3, which is not the case for the meshes tested. However, it was considered that the solution with a coarser grid gave an unacceptable result. The numerical uncertainty for the pressure loss is 4.7%, which could be improved, though the limited computational capacity precluded further analysis and the solution is said to be grid independent. As a grid convergence test is a computationally demanding task, it is assumed that the grids created for the various design changes can be said to be mesh independent. Therefore, the same approach to the grid generation is employed as in grid No. 1 with $4.568 \cdot 10^6$ cells, when design changes are made to the hot air chamber.

5. Results and discussion

If the ambient air and the hot air from the line burner is properly mixed the temperature of the combined air stream was found to be 152 °C. By further mixing the heated ambient air with the recirculation air the temperature of the outlet air was found to be 92 °C.

5.1. Original design

The temperature distribution in the outlet ducts from the original design is shown in Fig. 3. It can be seen that the temperature in the centre ducts lie in the range of 100–150°C. The air temperature, in the first four rows of the vertical ducts, is only 5–15 K above the recirculation air temperature. This indicates that the mixing between the heated air and the recirculation air is not satisfactory.

It was investigated what was the cause the poor mixing of the recirculation air and the heated air. It was found that the heated

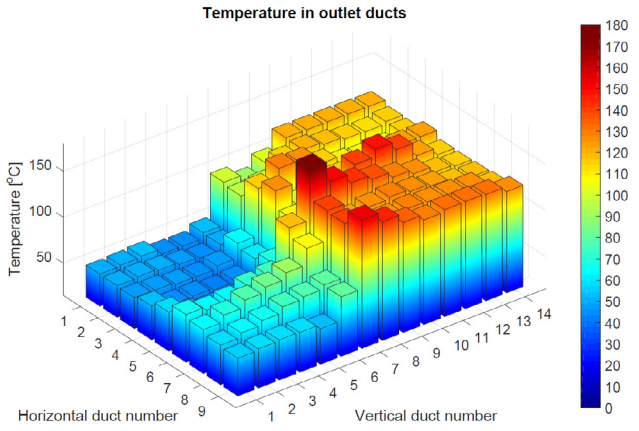

Fig. 3. Temperature distribution in outlet ducts of original design.

air was clinging to the outer wall of the mixing chamber, and thereby not mixing with the cooler recirculation air. In Fig. 4 it is can be seen, that the baffle above the recirculation sub-chamber causes a large separation zone, where the low pressure causes the recirculation air to wrap around to the lower outlets.

It is clear from the temperature distribution in the outlet ducts, shown in Fig. 3 and the temperature contour with a velocity vector overlay in Fig. 4, that the baffles at the top of the sub-chambers restrict the mixing of the heated air stream and the recirculation air. Furthermore, the large separation zone created also contributes to a poor temperature distribution in the outlets. With a pressure loss of 700 Pa in the hot air chamber, which is much larger than desired, the first change to the design should have the aim of reducing the pressure loss. Depending on the reduction in pressure loss it is then possible to change the configuration of the baffles in the mixing chamber. With the guide vanes at the ambient air inlet in the original design being straight plates with a 135° bend, and the inlet being above the bottom of the guide vane chamber, it was observed that this configuration caused large separation zones, which in effect cause an increase in pressure loss. Therefore, a study of the guide vanes was conducted.

5.2. Guide vane designs

One of the main requirements of the new dryer is, that the velocity of the air passing over the burner must be uniform to ensure an even heat distribution in the flow. Furthermore, it is required to have a maximum velocity in the range of 10–12 m/s, as larger velocities will cause an unstable flame in the burner. Large flow separation zones form behind the flat plated guide vanes, installed in the original hot air chamber design, which cause a pressure loss. In an effort to reduce the total pressure loss in the hot air chamber, and to have a uniform flow around the burner, three new designs of guide vanes have been tested and compared to the original. The effect of installing guide vanes in various systems, to obtain a better flow uniformity and a reduced pressure loss, has been reported widely in the literature [12–14].

In order to design new guide vanes, in a consistent manner, it is assumed that the ambient air flows through a 90° sharp elbow bend with an expansion. The three new guide vane designs, including the original, can be seen in Fig. 5. The short guide vanes were designed using expressions from [15,16]. The long guide vanes were constructed using the same design, as the short guide vanes, but with extended lengths.

5.2.1. Uniformity of flow

To assess the uniformity of the flow around the burner, the uniformity index (UI), γ, can be applied. The UI has been utilised to indicate the degree of flow distribution in automotive catalytic converters [17]. The UI applied in this study describes how well a given flow, through a cut plane, resembles a plug flow. The UI can be written as [18]:

$$\gamma = 1 - \frac{1}{2} \cdot \left(\sum_{i=1}^{n} \frac{A_i}{A_{tot}} \cdot \frac{|v_i - \bar{v}|}{\bar{v}} \right) \tag{21}$$

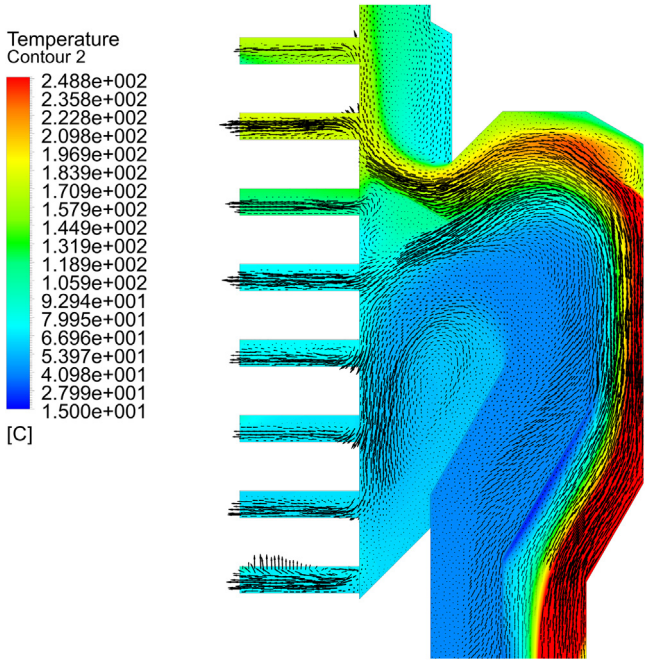

Fig. 4. Temperature contour with velocity vector overlay, of the mixing chamber for the original design.

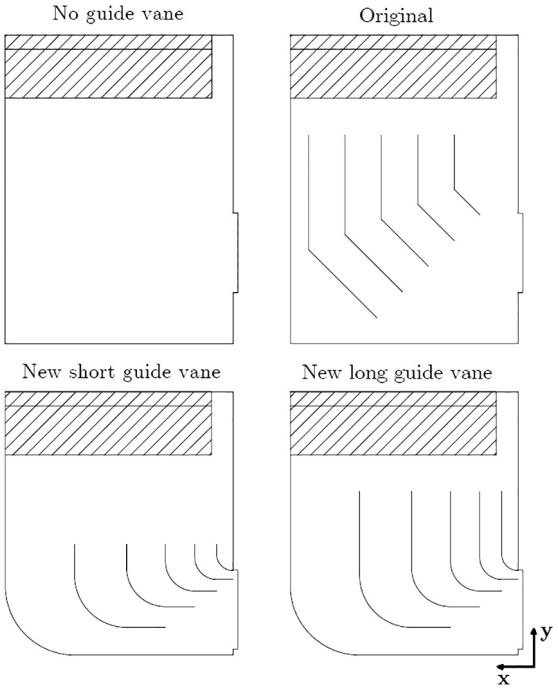

Fig. 5. Sketch of the four different guide vane designs, where a) indicate the axial fan inlet and b) indicate the burner.

where γ is the uniformity index, n is the number of cells in the cut plane, A_i is the area of the individual cell in the cut plane, A_{tot} is the total area of the cut plane, v_i is the velocity magnitude in the individual cell in the cut plane and $\bar{v}$ is the mean velocity in the cut plane.

The value of γ ranges between 0 and 1, where 1 indicates a uniform flow, and zero corresponds to $v_i = 0$ in all but a cell point.

5.2.2. Results of different guide vane designs

In Fig. 6 the mean velocity profiles at the line burner for the four designs: no guide vanes, original guide vanes, curved guide vanes (New short GV) and extended length of curved guide vanes (New long GV), are shown.

It can be seen that the velocity for the design with no guide vanes increases towards the centre of the burner sub-chamber. This is expected, as the flow cannot make an abrupt turn, when it reaches the expansion after the inlet. The velocity profiles of the original design and new design with elongated guide vanes, both have a jagged profile because the distance between the burner and the top of the guide vanes is too short for the flow to become fully-developed. The uniformity of the flow at the line burner and the pressure loss over the domain are shown in Table 4.

From the velocity profiles in Fig. 6, and the uniformity and pressure losses in Table 4, it is clear that the new design with short guide vanes is the best choice for further development, as it has the lowest pressure loss combined with a high uniformity of the flow around the line burner. Therefore, it was implemented in all further simulations of the hot air chamber.

It was seen in Fig. 3, that the original design of the hot air chamber did not produce a uniform temperature distribution in the outlet ducts, which is the main objective of this study. Therefore, design changes to the hot air chamber were conducted to improve the mixing of the heated ambient air and recirculation air.

5.3. Nozzle implementation

It is seen in Figs. 3 and 4 that the temperature and flow distributions are uneven and that the heated ambient air predominantly moves near the outer walls of the chamber. To counteract this flow behaviour, the position, of the recirculation and burner sub-chambers, is shifted. Furthermore, the baffle at the exit of the burner sub-chamber is angled to resemble that of a nozzle. Baffles are used in a variety of applications, such as improving the mixing of materials, directing fluid flow and increasing the heat transfer rate in heat exchangers and flow channels [19–21]. The purpose of the baffles at the end of the sub-chambers is to induce mixing between the two air streams and to control their flow directions. The purpose of forcing the air through the baffle, resembling a nozzle, is to ensure that the recirculation air flow does not remain along the outer wall, but is instead mixed with the heated ambient air. Furthermore, the angle of the baffle plate at the burner sub-chamber is reduced by 20° in order to increase the velocity of the heated air by a factor of two relative to the recirculation air. In Fig. 8 the design changes, of the hot air chamber, is seen.

A uniform temperature and flow distribution was, however, not achieved by implementing the above design changes. Instead of having the predominantly hot air at the top outlet sections and cooler at the bottom, the hot air is primarily entering the bottom sections and the cooler air at the top sections. This is apparent in Fig. 7. In addition, the pressure loss is significantly higher due to the nozzle at the outlet of the burner sub-chamber.

Table 4
Uniformity of v-velocity at the line burner and pressure losses for the four designs.

Design	Pressure loss [Pa]	Uniformity γ
No GV	613	0.708
Original	700	0.737
New short GV	630	0.804
New long GV	656	0.776

5.4. Flow obstruction implementation

The implementation of a nozzle at the end of the burner sub-chamber and shifting the position of the recirculation and burner sub-chambers had no effect on improving the temperature and flow distribution at the outlet ducts, as seen in Fig. 7. Consequently, a new hot air chamber design was analysed. This alternative design is inspired by an optimised design of an existing continuous flow dryer. The main feature of this design consists of flow obstructions installed to accelerate mixing of the two air streams. U-shaped plates are placed over the burner in a cross pattern to increase turbulence in the heated ambient air flow. The burner sub-chamber is connected to the recirculation sub-chamber by the means of air ducts, which forces the heated ambient air to mix with the recirculation air, before it is led through to the outlet ducts. The design, of the hot air chamber with flow obstructions implemented, is shown in Fig. 9. By performing these design changes the temperature distribution at the outlet ducts were very uniform and this is seen in Fig. 10. However, the implementation of the flow obstructions caused a significant pressure loss in the hot air chamber.

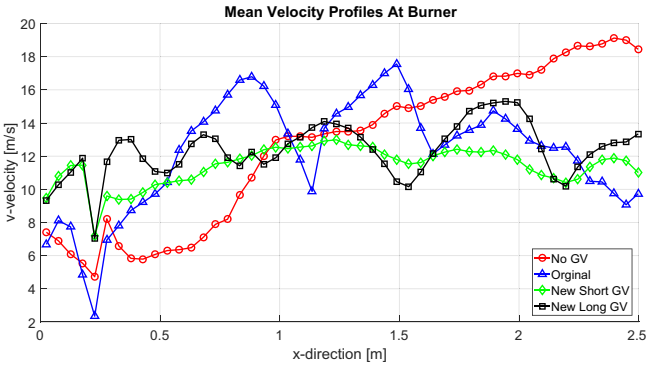

Fig. 6. Velocity profiles for v-velocity at the line burner. The x-direction is shown in Fig. 5.

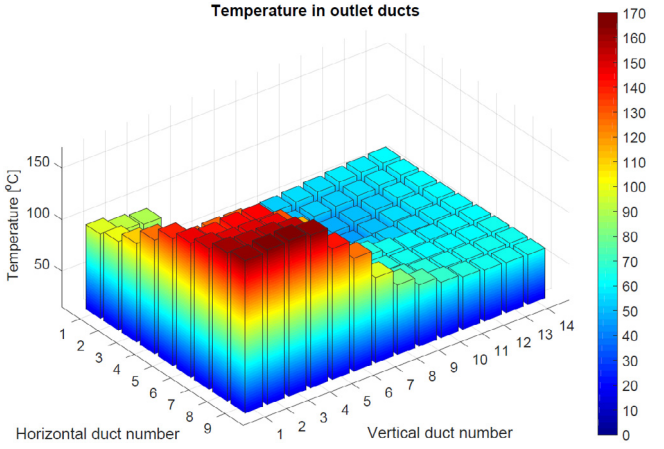

Fig. 7. Temperature distribution at the outlet ducts for the design with nozzle implementation.

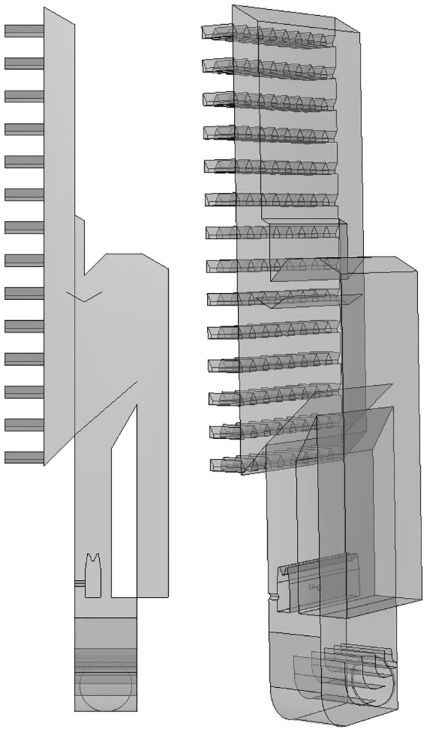

Fig. 8. Cross sectional views of the hot air chamber with nozzle implementation.

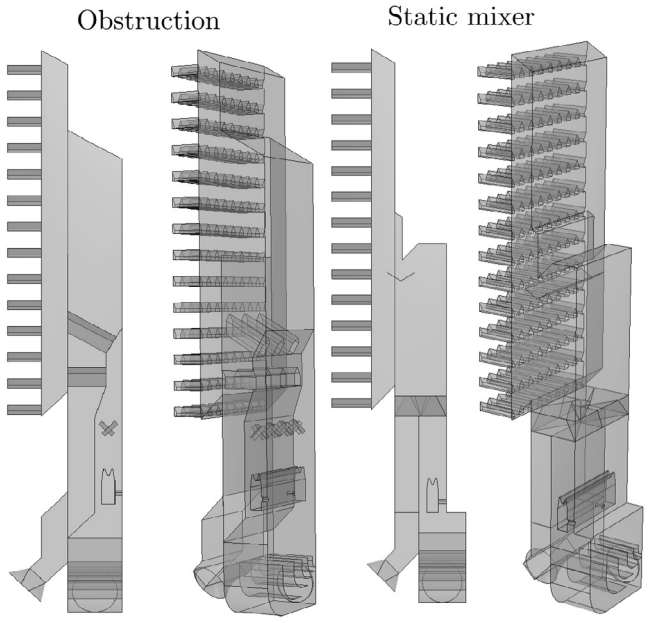

Fig. 9. Geometry of the hot air chamber with the flow obstructions and the static mixer implemented, respectively.

5.5. Static mixer implementation

With the large pressure loss in the obstruction design, a new design approach was analysed. Inspiration was gathered from existing mixing devices and in particular static mixers. Static mixers are especially used in the process industry in a variety of applications, such as single-phase and two-phase continuous co-current gas–liquid dispersions, and as mass transfer enhancement [22,23].

A static mixer was designed and implemented at the outlets of the sub-chambers of the burner and the recirculation air. The design of the static mixer is inspired by existing mixers on the markets, such as the HEV static mixers from Chemineer Inc., LPD and LLPD motionless mixers from Ross Engineering Inc. and the pitch blade turbine impellers from Fusion Fluid Equipment. The aim is to test if the use of static mixers in fact improve the mixing of the two air streams. For that reason, the design of the mixer is kept simple and also to allow for a simpler mesh generation process. The geometry of the static mixer comprises of six flat plates angled at 25° in a propeller type shape. In Fig. 11 the geometry, of the designed static mixer, is seen. A cross sectional view, of the hot air chamber with static mixers implemented, can be seen in Fig. 9.

In Fig. 12 the temperature distribution at the outlet sections, with the static mixer installed, is shown. It is evident, that the design changes resulted in an even mixing between the recirculation and heated ambient air streams. This is especially apparent in the vertical outlet sections number 4–6, where significant temperature peaks occur. As improper mixing between the air streams from the recirculation and burner sub-chambers occur, the heated ambient air flows mainly into outlet sections 4–6, which causes the high temperature peaks. That said, there is a fairly uniform distribution from the vertical outlet sections 7–14.

In Fig. 12 the temperature distribution at the outlet sections, with the static mixer installed, is shown.

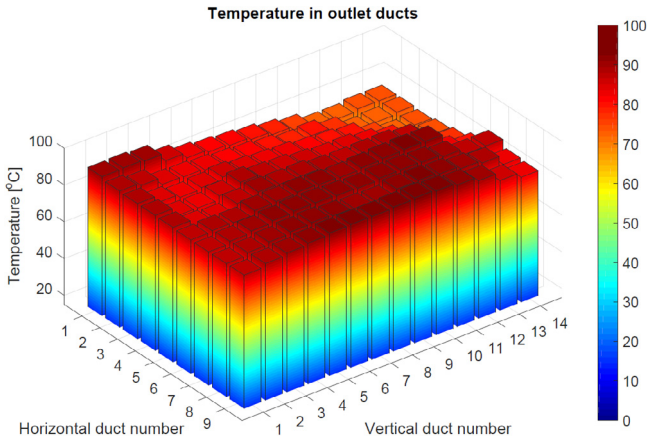

Fig. 10. Temperature distribution at the outlet ducts for the design with flow obstruction implementation.

5.6. Design evaluation

In an ideal design the temperatures should only vary ±5 K from the mean temperature in the outlet ducts. To assess the temperature distribution at the outlets in the different designs, the mean absolute deviation (MAD) of the temperature distribution in the outlet ducts have has calculated. The pressure losses and MAD, of the five different designs investigated, are shown in Table 5.

As previously shown it is clear that the implementation of the new guide vanes, at the ambient air inlets in the original design, reduced the pressure loss in the hot air chamber significantly

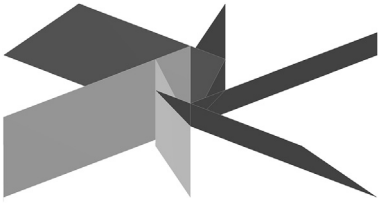

Fig. 11. Design of the developed static mixer.

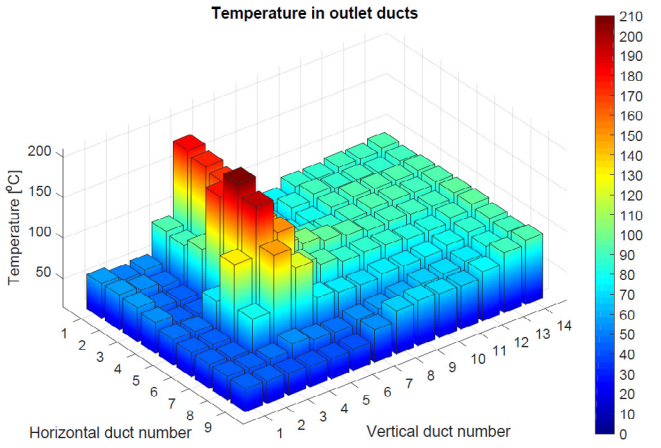

Fig. 12. Temperature distribution in the outlet ducts of the design with static mixers implemented.

Table 5
Pressure losses and mean absolute deviation for the five designs.

Design	Pressure loss [Pa]	Mean absolute deviation [K]
Original	700	31.7
Original new guide vane	630	24.8
Nozzle	1282	31.4
Flow obstruction	2962	4.57
Static mixer	485	22.9

compared to the original guide vane design. Furthermore the implementation of the new guide vanes decreased the MAD from MAD from 31.7 K to 24.8 K.

In addition, it was found that the flow of the heated air *clung* to the outer wall. In an effort to break the flow running along the outer wall the position, of the burner sub-chamber and the recirculation air sub-chamber, was exchanged, and the angle of the baffle above the burner sub-chamber was reduced to increase the velocity of the air. These changes to the design resulted in an increased size of the separation zone behind the baffle above the burner sub-chamber. This, in effect, resulted in a reduced mixing of the recirculation air and the heated ambient air, and it can be seen, in Table 5, that the design has the largest MAD-value of all the designs that have been analysed. Furthermore, the implementation of the nozzle increased the pressure loss to 1282 Pa, which is double that of the original design.

After the analysis of the original and the nozzle design, it was clear that the baffles above the sub-chambers did not improve the mixing of the heated ambient air and the recirculation air. Therefore, a new design where the baffles are substituted by a series of ducts, which force the heated ambient air into the recirculation stream, was analysed. As it was shown in Fig. 10 the temperature distribution in the outlet ducts is essentially uniform, and this is further confirmed with a MAD of only 4.57 K, which is lower than the goal set, which was ±5 K. However, it was found that obtaining an even temperature distribution comes at the expense of a pressure loss of 2962 Pa.

In the four designs tested it was observed that either the temperature distribution were too uneven or the pressure loss was too large. Based on these observations it was investigated, whether the implementation of static mixers could improve the mixing of the recirculation air and the heated ambient air, while retaining a reasonable pressure loss. From the simulation results it was seen that the implementation of the static mixers did increase the mixing compared to the original design especially in the top half of the outlets. Additionally, the MAD decreased from 24.8 K, in the original design, to 22.9 K. It was also found that the pressure loss was reduced from 630 Pa in the original design to 485 Pa with the implementation of the static mixers.

6. Conclusion

A CFD model was developed to study the air flow in the hot air chamber of a newly designed continuous flow grain dryer. The main focus of the study was to model the air flow and to improve the mixing of the recirculation and heated ambient air streams. It was concluded that the original design resulted in poor mixing, and thereby an uneven temperature distribution at the outlet sections. Considering, that a varied temperature distribution at the outlet sections can lead to improper drying or damage to the end-product, various design changes were analysed to improve these parameters. New guide vanes were designed to reduce the pressure loss and to increase the uniformity of the flow entering the burner sub-chamber. Following the successful reduction of the pressure loss the new guide vanes were implemented in the various hot air chamber designs. The design with the nozzle implemented did not significantly improve the mixing of the two air streams, however it led to a notably increased pressure loss of 1214 Pa. The effect of installing multiple flow obstructions in the hot air chamber was a highly uniform temperature distribution at the outlet sections and a MAD value of only 2.72 K, which is within the range of the ±5 K goal, though the high flow uniformity came at the price of a significantly increased pressure loss of 2859 Pa, which is considerably higher than that in the current range of continuous flow dryers. The design, using static mixers, slightly improved the uniformity of the flow entering the outlet ducts compared to nozzle design, as it led to MAD of 24.1 K. Including static mixers and removing the baffle at the end of the recirculation and burner sub-chamber, led to a pressure loss of 399 Pa, which was the lowest of all the hot air chamber designs. The static mixer design can serve as a promising conceptual design for further optimisation and improvement of the hot air chamber.

References

[1] G.C. Mrema, L.O. Gumbe, H.J. Chepete, J.O. Agullo, Rural structures in the tropics – design and development, The Technical Centre for Agricultural and Rural Cooperation, 2011, iSBN: 978-92-5-107047-5.
[2] S. Giner, R. Mascheroni, M. Nellist, Cross-flow drying of wheat: a simulation program with a diffusion-based deep-bed model and a kinetic equation for viability loss estimations, Drying Technol. (1996) 1625–1671.
[3] S.A. Giner, D.M. Bruce, S. Mortimore, Two-dimensional simulation model of steady-state mixed-flow grain drying, Agric. Eng. 71 (1998) 37–50.
[4] Y. Amanlou, A. Zomorodian, Applying cfd for designing a new fruit cabinet dryer, J. Food E 101 (1). doi: https://doi.org/10.1016/j.jfoodeng.2010.06.001.
[5] F. Romn, V. Strahl-SchSfer, O. Hensel, Improvement of air distribution in a fixed-bed dryer using computational fluid dynamics, Biosyst. Eng. 112 (4) (2012) 359–369.
[6] H.K. Versteeg, W. Malalasekera, An Introduction to Computional Fluid Dynamics – The Finite Volume Method, Pearson, 2009.
[7] F.R. Menter, Zonal two equation k-w turbulence models for aerodynamic flows, AIAA doi: https://doi.org/10.2514/6.1993-2906.
[8] ANSYS, ANSYS Meshing Users Guide, 17th Edition (Aug. 2016).
[9] P.J. Roache, Perspective: a method for uniform reporting of grid refinement studies, J. Fluids Eng. 116 (1994).
[10] I.B. Celik, U. Ghia, P.J. Roache, C.J. Freitas, H. Coleman, P.E. Raad, Procedure for estimation and reporting of uncertainty due to discretization in cfd applications, J. Fluids Eng. 130 (2008).
[11] L. Zhuanga, H. Guob, G. Daia, Z. liang Xua, Effect of the inlet manifold on the performance of a hollow fiber membrane module-a cfd study, J. Membr. Sci. 526 (2017) 73–93.
[12] J. Haskew, M. Sharif, Performance evaluation of vaned pipe bends in turbulent flow of liquid propellants, Appl. Math. Model. 21 (1) (1997) 48–62, https://doi.org/10.1016/S0307-904X(96)00121-7.
[13] P. Modi, S. Jayanti, Pressure losses and flow maldistribution in ducts with sharp bends, Chem. Eng. Res. Des. 82 (3) (2004) 321–331, https://doi.org/10.1205/026387604322870435.

[14] T.-M. Liou, H.-L. Lee, C.-C. Liao, Effects of guide-vane number in a three-dimensional 60-deg curved side-dump combustor inlet, J. Fluids Eng. 123 (2) (2001) 211–218, https://doi.org/10.1115/1.1358843.
[15] I.E. Idelchik, Handbok of Hydraulic Resistance, 2nd Edition., Springer-Verlag, 1986.
[16] M. Kawano, Elbow provided with guide vanes, Google Patents, eP Patent 0,667,460 (Apr. 2001). https://www.google.com/patents/EP0667460B1?cl=en.
[17] G.W. Lee, M.Y. Kim, Investigation of the flow characteristics in a catalytic muffler with perforated inlet cone, Int. J. Mech., Aerosp., Ind., Mech. Manuf. Eng. 8 (5) (2014).
[18] D.A. Mitchell, T. Szailer, S.C. Alonzo, C. Newton, Uniformity index performance evaluation in an scr aftertreatement system, patent no. WO2014066214 A1 (2014). https://www.google.com/patents/WO2014066214A1?cl=en
[19] F. Yu, G. Zhou, J. Xu, W. Ge, Enhanced axial mixing of rotating drums with alternately arranged baffles, Powder Technol. 286 (2015) 276–287, https://doi.org/10.1016/j.powtec.2015.08.032.
[20] P. Promvonge, S. Sripattanapipat, S. Kwankaomeng, Laminar periodic flow and heat transfer in square channel with 45 inline baffles on two opposite walls, Int. J. Therm. Sci. 49 (6) (2010) 963–975, https://doi.org/10.1016/j.ijthermalsci.2010.01.005.
[21] A.E. Maakoul, A. Laknizi, S. Saadeddine, A.B. Abdellah, M. Meziane, M.E. Metoui, Numerical design and investigation of heat transfer enhancement and performance for an annulus with continuous helical baffles in a double-pipe heat exchanger, Energy Convers. Manage. 133 (2017) 76–86, https://doi.org/10.1016/j.enconman.2016.12.002.
[22] A. Couvert, C. Sanchez, I. Charron, A. Laplanche, C. Renner, Static mixers with a gas continuous phase, Chem. Eng. Sci. 61 (11) (2006) 3429–3434, https://doi.org/10.1016/j.ces.2005.11.040.
[23] J.G. Khinast, A. Bauer, D. Bolz, A. Panarello, Mass-transfer enhancement by static mixers in a wall-coated catalytic reactor, Chem. Eng. Sci. 58 (36) (2003) 1063–1070. 17th International Symposium of Chemical Reaction Engineering (IS CRE 17).doi: https://doi.org/10.1016/S0009-2509(02)00648-6.